Research article **Open Access**

Kelvin Chung*, Timothy J. Karle[a], Asma Khalid, Amanda N. Abraham, Ravi Shukla, Brant C. Gibson, David A. Simpson, Aleksandra B. Djurišic, Hiroshi Amekura and Snjezana Tomljenovic-Hanic

Room-temperature single-photon emission from zinc oxide nanoparticle defects and their *in vitro* photostable intrinsic fluorescence

DOI 10.1515/nanoph-2015-0138
Received November 5, 2015; revised April 5, 2016; accepted April 6, 2016

Abstract: Zinc oxide (ZnO) is a promising semiconductor that is suitable for bioimaging applications due to its intrinsic defect fluorescence. However, ZnO generally suffers from poor photostability. We report room-temperature single-photon emission from optical defects found in ZnO nanoparticles (NPs) formed by ion implantation followed by thermal oxidation in a silica substrate. We conduct a thorough investigation into the photophysics of a particularly bright defect and identify other single emitters within the NPs. Photostability was observed when the NPs were removed from the growth substrate and taken up by skin cells for *in vitro* imaging.

Keywords: zinc oxide; optical defects; single-photon emitters; intrinsic fluorescence; HaCaT cells.

[a]Current address: The Florey Institute of Neuroscience and Mental Health, Parkville, Victoria 3052, Australia.
***Corresponding author: Kelvin Chung,** School of Physics, The University of Melbourne, Parkville, Victoria 3010, Australia, e-mail: kelvinc@student.unimelb.edu.au
Timothy J. Karle, Asma Khalid, Brant C. Gibson, David A. Simpson and Snjezana Tomljenovic-Hanic: School of Physics, The University of Melbourne, Parkville, Victoria 3010, Australia
Amanda N. Abraham and Ravi Shukla: School of Applied Sciences, RMIT University, Melbourne, Victoria 3001, Australia
Aleksandra B. Djurišic: Department of Physics, The University of Hong Kong, Pokfulam Road, Hong Kong
Hiroshi Amekura: National Institute for Materials Science (NIMS), 3-13 Sakura, Tsukuba, Ibaraki 305-0003, Japan

1 Introduction

In the last few years, the study of metal oxide nanoparticles (NPs) has become a distinctive subject of research. Studies on both the physical implementations of these particles and their applications are undertaken. This increased interest is driven by numerous applications of metal oxide materials in the industry, medicine, information technology, energy storage, sensing, and many others [1–3].

In particular, zinc oxide (ZnO) itself is widely used (several 100,000 tons/year) [3] in many industrial applications. ZnO is a direct wide bandgap ($E_g \approx 3.3$ eV at room temperature) material [4] with many growth methods, including magnetron sputtering [5, 6], chemical vapour deposition [7], molecular beam epitaxy [8, 9], and hydrothermal synthesis [10, 11], to name a few [12]. This enables many different morphologies, e.g. thin films and nanostructures such as wires [13], rods [7, 11, 13], combs [14], and particles [15], for a variety of applications. The fluorescence properties of ZnO have also been extensively studied and show a strong emission peak in the UV, due to the recombination of free excitons, and broadband emission in the visible region, attributed to defects within the crystallographic structure [16–18].

These atomic scale defects within wide bandgap semiconductors have increasingly attracted attention as sources of photonic and electronic qubits at room temperature. A wide bandgap isolates the defects from a significant thermal population and from the activation of nonradiative mechanisms. Very few systems demonstrate room-temperature single-photon emission and these include diamond [19], silicon carbide defects [20], and CdSe/ZnS quantum dots [21]. More recently, ZnO has been added to this list where its structure has been observed to host defect-related single emitters at room temperature [22–26].

The origin of the defect luminescence of ZnO is the subject of intense debate. In the visible emission spectrum, different defects are attributed to the green, yellow, and orange-red emissions [16, 27]. The green emission band is attributed to a variety of defects including singly ionised oxygen vacancies [28–31], antisite oxygen [17, 32, 33], zinc interstitials [34], and zinc vacancies [35]. Given that there is no consensus in the mechanism for green emission, this shows how highly debated the origins of the luminescence are for ZnO [36, 37]. Similarly, for yellow and orange-red emissions, there are many competing hypotheses, but the community has mainly attributed oxygen interstitials [34, 38, 39] as the primary candidate. More recently, red emission has been attributed to negatively charged zinc and positively charged oxygen vacancies within ZnO nanocrystals [40] and zinc interstitial-oxygen vacancy complexes or zinc-oxygen divacancies in ZnO single crystals [41]. Often, the contradictory results for ZnO defect emission may be attributed to the plethora of growth conditions that inevitably control what defects are introduced into the crystallographic structure of ZnO [4].

Room-temperature single-photon emission from optical defects within ZnO NPs has been observed recently [22, 23], adding another candidate to the list of single-photon sources. Single-photon emission was overlooked for decades because material scientists generally perform ensemble (i.e. bulk) measurements [42, 43], which end up sampling multiple optical defects. A thorough knowledge of the growth conditions and introduced defects coupled with high-resolution fluorescence microscopy, alongside density functional theory calculations, can yield the correct chemical origin of the defects. With mature fabrication techniques for various morphologies, unique optical properties, and now single-photon emission, ZnO is an extraordinary material that has found electronic, optoelectronic, and MEMS applications [4, 44]. Furthermore, the therapeutic properties of ZnO have been well explored for many biomedical applications, which include anticancer [45, 46] and antibacterial [47, 48] agents. Within the bioimaging realm, NPs have been touted to pioneer the understanding of biological processes at the molecular level [49]. However, photostability has always been an issue. Without further modification, previous work on ZnO defects showed blinking photodynamics [22, 23, 25] and broad red photoluminescence (PL) [22–25].

In this paper, we present single-photon emission from defects in ZnO NPs formed by Zn ion implantation followed by thermal oxidation [42, 43, 50]. We observe red defect emissions under 532 nm excitation at room temperature, where the defects exhibit blinking characteristics with occasional photostability. Furthermore, ZnO NPs were also removed from the silica substrate, and characterised again, with the motivation of using ZnO as a promising candidate for bioimaging [51]. We show that these ZnO NPs were able to be taken up by human epidermal keratinocyte cells, resulting in photostable emission from the defects above cellular autofluorescence.

2 Materials and methods

2.1 Fabrication of ZnO NPs

ZnO NPs were created by ^{64}Zn ion implantation at 60 keV with a fluence of 1.0×10^{17} ions/cm^2 followed by the thermal oxidation of silica glass [42, 43]. At an oxidation temperature of 600°C, most of the Zn ions are converted into the Zn metal and remain in this phase. At temperatures between 700°C and 800°C, the Zn metal begins to convert to ZnO and smaller NPs appear within the substrate with larger NPs aggregating on the surface [42, 43].

2.2 Confocal microscopy

ZnO NP samples were investigated with a home-built scanning confocal microscope, which consists of an Nd:YAG frequency-doubled 532 nm continuous wave (CW) laser excitation focused on the sample with a 100× air objective (NA=0.95). The system has a lateral resolution-limited spot size of approximately 0.28 μm. The fluorescence signal is recollected through the objective and filtered by a 560 nm long-pass filter. It is incident upon a multimode optical fibre, which acts as the confocal pinhole. The confocal microscope has two main configurations: (1) Hanbury-Brown Twiss (HBT) correlation measurements and (2) spectrometry. In configuration 1, the signal was split between two fibre-coupled single-photon avalanche diodes set up for HBT measurements. In configuration 2, the signal was coupled into a spectrometer and detected by a CCD camera (Acton SpectraPro 2300i with Pixis100 camera).

2.3 Ensemble PL

The ensemble PL was excited by a 325 nm line from a CW mode He-Cd laser (Kinmon, IK-3301R-G) with an excitation spot of 0.2 mm in diameter. The pump power was 3 mW. Luminescence was collected by a concave mirror, guided to a 32 cm monochromator (Horiba Jobin Yvon, iHR320)

through a 370 nm long-pass filter, and then detected by a cooled CCD detector (Horiba Jobin Yvon, Synapse).

2.4 Removal of ZnO NPs from silica substrate

This was done by placing the sample into isopropyl alcohol (IPA). A scalpel was used to scratch the surface of the sample to remove the NPs for dispersion into the IPA. This mixture was then pipetted onto a bare Si chip (5×5 mm^2) and spun to evaporate the IPA, which allows the NPs to settle onto the Si surface. This sample was then investigated using confocal microscopy (see Section 2.2).

2.5 Cell preparation

The material list to prepare the cells was as follows: RPMI 1640 medium, sterile tissue culture grade distilled water, phosphate-buffered saline (PBS) and 10,000 U/ml penicillin-streptomycin (Life Technologies Australia), poly-L-lysine (Sigma-Aldrich), and foetal calf serum (FBS; Interpath Services). Transformed human skin keratinocyte (HaCaT) cells were maintained in RPMI 1640 medium supplemented with 10% FBS and 1% penicillin-streptomycin. The cells were maintained in a humidified incubator with 5% CO_2 at 37°C.

ZnO NPs were removed in the same procedure as described in Section 2.4, with the difference of using distilled water instead of IPA. The solution was tested on the cells grown in cell chambers on a slide. The cell chambers were treated with 0.01% (w/v) poly-L-lysine in sterile distilled water for 5 min as per the manufacturer's instructions. Poly-L-lysine was aspirated and the chambers were washed twice with sterile distilled water and allowed to dry for 2 h before seeding the cells.

Some ZnO NPs were filtered through a 0.22 μm filter to remove the bigger particles, which were possibly glass chips from scraping the NPs off the slide they were synthesised on. The cells were treated with both filtered and nonfiltered NPs for 16 h, washed in PBS, and imaged (see Section 2.6 for further details).

2.6 Wide-field imaging of NPs taken up by cells

For the optical characterisation of ZnO NPs in cells, we used wide-field fluorescence microscopy. This experiment uses the intrinsic fluorescence from ZnO NP defects for *in vitro* imaging. Initially, the cells were incubated in RPMI 1640 medium inside the glass bottom of cell chambers at 37°C. NPs were then introduced and the cells were placed in a cell culture incubator overnight to enable the maximum cellular uptake of NPs.

Wide-field imaging was performed for cells alone and with ZnO NPs. This was done with an inverted wide-field confocal fluorescence microscope (Nikon, Eclipse Ti-U). A 532 nm laser was used with an excitation power density of 20 W/mm^2. A telescope was used to expand the laser beam before focusing the excitation onto the back aperture of a 100× 1.45 NA (Nikon) oil immersion objective with a focusing lens (f=300 mm). This provided an 80×80 μm^2 field of view. Wide-field fluorescence images were captured with an sCMOS camera (Andor, Neo). Imaging was performed at 37°C by a temperature-controlled environmental chamber around the microscope. Before imaging, the culture medium was washed and replaced with PBS to avoid unwanted background fluorescence associated with the cell culture medium.

3 Results and discussion

3.1 Optical characterisation of ZnO NPs on top of silica substrate

ZnO NPs were fabricated via ion implantation followed by thermal oxidation (see Section 2.1 for more details). We investigated three samples annealed at temperatures of 600°C, 700°C, and 800°C. ZnO NPs are expected to form at 700°C and 800°C and can be visually confirmed as the sample becomes transparent. ZnO NPs grow inside and on the surface of the silica substrate. The NPs vary in size, generally increasing with higher annealing temperatures.

The samples were optically characterised using a home-built scanning confocal microscope (see Section 2.2). Figure 1 shows representative confocal scans of the 700°C annealed ZnO NP sample. The confocal scans reveal a high density of spatial and spectrally distinct fluorescing features originating from point defects within ZnO, which can be seen in Figure 1A. The density of features was dependent on the spatial (in-plane) position of the focus spot and fine features can be readily solved. The count rates for the distinct features were found to range from 13 to 250 kc/s, for a power range of 0.5–1.3 mW, which indicates that optical defects in ZnO can be relatively bright emitters. The defect count range refers to distinct and resolvable bright spots on the confocal scans.

The spectral characteristics of the single-photon emitters were investigated in the visible spectral range.

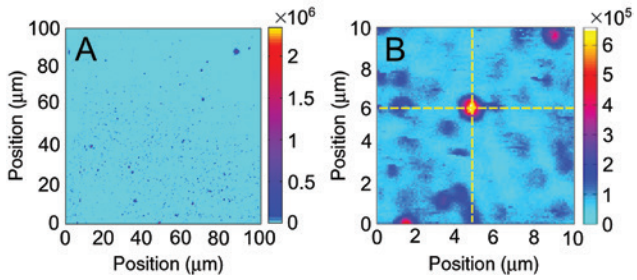

Figure 1: Archetypal confocal scans of the ZnO NP sample annealed at 700°C.
(A) 100×100 μm² scan and (B) 10×10 μm² scan showing a bright emitter found on the sample. The emitter at the centre of the cross hair at coordinates of (x, y)=(5, 6) μm was optically characterised and the results are presented in this text. The colour bar on the side represents the count rate at the detector (units of c/s).

The spectrum of the single-photon emitters in ZnO NPs is important in establishing the origins of the optical defects. High-resolution microscopy will assist in identifying the origins of the visible emission peaks resulting from individual emitters. This is not feasible with ensemble measurements, as the spot size (≈0.2 mm; see Section 2.3) is approximately 700 times larger than the individual defect confocal resolution (≈280 nm; see Section 2.2). Therefore, in the bulk measurement, the total fluorescence from many optically active defects contribute to the broad visible band. Figure 2A and B shows an ensemble and individual defect PL spectra from the ZnO NP sample. Figure 2B shows that we are able to address fluorescence at the defect level and resolve visible band emission peaks within the ensemble PL spectrum of Figure 2A.

The red coloured plot in Figure 2B is the spectrum of a particularly bright emitter shown in Figure 1B (130 kc/s at pump power=185 μW) that the optical characterisation was conducted on. The emission spectrum shows a central peak at 631 nm with a subtle peak at 690 nm. There was also significant fluorescence occurrent at wavelengths below 600 nm. The abrupt leading edge was due to a 570 nm long-pass filter. The emission range matches the previous reports by Morfa et al. [22], Choi et al. [23, 24], and Neitzke et al. [26], where their single defects also showed broad red fluorescence. In this study, the results reveal that ZnO optical defects have distinct and resolvable emission peaks compared to the aforementioned work at room temperature. It must be noted that Neitzke et al. [26] also observed a very narrow zero phonon line at 580 nm when they measured their ZnO optical defects at cryogenic temperatures, which greatly suppresses their phonon sideband emission from 600 to 750 nm.

A range of different emission peaks were observed for antibunching defects within the ZnO NP sample. From the defect spectra, the bandwidth of the emission was observed to lie between 580 and 850 nm. ZnO NPs were grown in an oxygen-rich environment that could give rise to oxygen interstitial defects into the ZnO structure [34, 38]. On the contrary, red emission has been attributed to zinc vacancy complexes [27]. For the red fluorescence, Morfa et al. [22] and Neitzke et al. [26] attributed it to the zinc vacancies as designated by Wang et al. [52]. Because we have observed quantum emission from various other emission peaks, zinc vacancies cannot be solely responsible for this phenomenon.

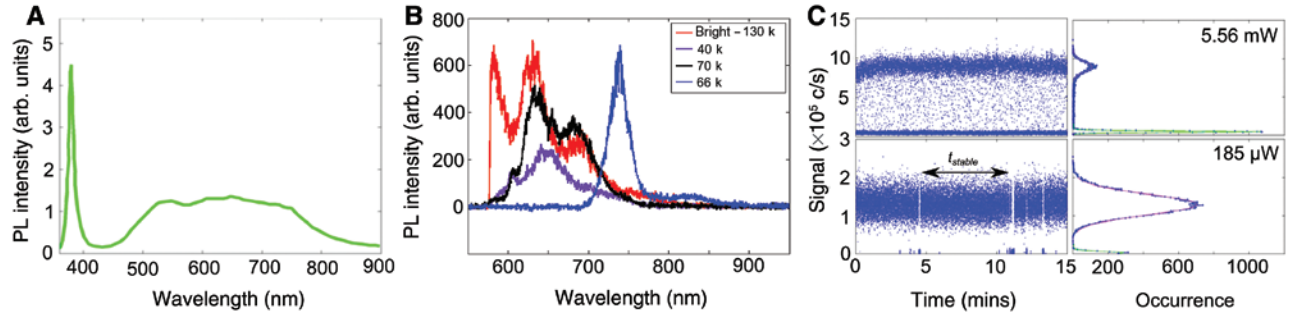

Figure 2: PL spectra of the ZnO sample annealed at 700°C.
(A) Bulk ensemble measurement with an excitation from a 325 nm HeCd laser (spot size≈0.2 mm; see Section 2.3). (B) Single defects with various emission peaks found on the sample with an excitation from a 532 nm Nd:YAG frequency-doubled laser (spot size≈280 nm). The red coloured plot is the spectrum for the bright emitter shown in Figure 1B with an average count rate of 130 kc/s at a pump power of 185±3 μW. The leading edge at 570 nm was due to the long-pass filter used within the experimental set-up. The other spectra were antibunching defects also found on the 700°C annealed ZnO sample differentiated by various count rates that were observed. (C) Count traces and histograms obtained for a low and high pump power, 185±3 μW and 5.56±0.03 mW, of the bright emitter shown in Figure 1B. The two levels registered in the detector (signal) are for the background and bright states of the emitter with no obvious grey state. For the low pump power of 185 μW, the bright state was observed to be active for more than 5 min (t_{stable}).

The spectral results reveal different emission peaks for the quantum emission. The multiple peaks could be due to fundamentally different defects. However, at this stage, we cannot assign an individual chemical origin responsible for the various emission peaks seen in the red fluorescence. This was also the conclusion for previous work by Choi et al. [23]. In a follow-up work [24], they postulated that their red fluorescence could be due to oxygen interstitials or zinc vacancy defects. At this juncture, a methodical study of optical defects as a function of fabrication method is needed to identify the origins.

The photostability of emitters is another characteristic requirement for quantum information science [53] and bioimaging [49]. The search for and engineering of a robust emitter found within an NP is crucial for this technology to become more widespread as an imaging modality. Figure 2C shows the time traces and histogram of counts for two different powers of 185 μW (Figure 2C, bottom) and 5.56 mW (Figure 2C, top) for the bright emitter shown in Figure 1B. For this particular defect, we observe the defect blinking between a bright and dark state even at high pump power.

The blinking frequency of the emitter increased, as a function of pump power, between background fluorescence and bright count levels. Interestingly, at a pump power of 185 μW, we observe infrequent blinking at some points in the time trace, and the emitter can be "on" for more than 5 min. The emitters in our ZnO sample exhibit comparable photodynamics, with extended periods of photostability, compared to previous work [22, 23, 25]. Choi et al. [23] have shown the prevention of photobleaching by polymethyl methacrylate (PMMA) encapsulation of their ZnO NPs with the cost of blinking characteristics. A follow-up work on electrically driven defects in ZnO NPs by Choi et al. [24] has also shown stable photodynamics. Neitzke et al. [26] also observed relatively stable emission from their ZnO NP optical defects at room temperature for a short period of time, in the order of tens of seconds to several minutes. We have observed a blinking defect, with intermediate dwell times in the bright state, within ZnO NPs without any encapsulation. The bright defect in Figure 1B was very unique, and under steady excitation, multiple hours of data acquisition were attainable before photobleaching occurred at high pump powers (>5.56 mW). It must be noted that the majority of the single defects were much more sensitive and did not show robust behaviour and readily photobleached at relatively low pump powers (hundreds of microwatts).

The bright single-photon emitter (Figure 1B) was further characterised by exploring the pump power dependence on its antibunching behaviour, which allows the intrinsic lifetime to be determined. Figure 3A shows the normalised $g^{(2)}$ data (with background correction [19, 54]) as a function of delay time τ for the bright emitter shown in Figure 1B. $g^{(2)}$ is measured as a function of pump power incident on the emitter within the range of 185 μW–5.56 mW, which has been offset vertically for clarity. The characteristic dip at zero delay time represents a decreasing probability of detecting two correlated photons in the HBT interferometer. An ideal single-photon source would result in $g^{(2)}(0)=0$, where the photon has taken a single path through one arm of the interferometer.

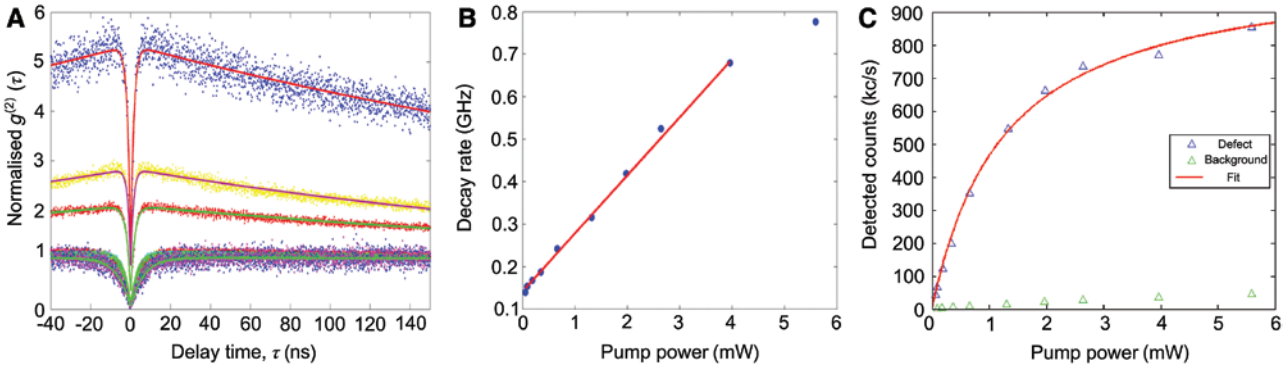

Figure 3: (A) Background-corrected $g^{(2)}$ histograms of the bright emitter in Figure 1B as a function of increasing pump power, which has been offset vertically. The range of pump powers is from 185 μW to 5.56 mW with increasing bunching behaviour observed at the "shoulders" of the antibunching dip for higher pump powers. (B) Excited state decay rates for a three-level model fit of the bright emitter [19, 54]. The intrinsic excited state lifetime of the emitter is approximately 7 ns. Data were fitted with a linear fit to extract the lifetime for low powers using the intercept of the reciprocal lifetime. The single point at the highest pump power of 5.56 mW does not follow this linear trend and indicates that, at high incident powers, additional terms may need to be included in the model. (C) Saturation curve for a bright emitter found on the sample. The blue diamonds and green triangles represent signal from the defect (background subtracted) and background, respectively. The red line represents fit of the emission rate as a function of pump power.

Another important property of a single-photon emitter is the lifetime of the excited state. We observed blinking behaviour, with protracted "on" states, for fluorescent emitters that exhibited antibunching, which is indicative of radiative emission behaviour. There also can be a non-radiative pathway for the relaxation of the electron from the excited state. The total system can be represented by a simplified three-level model fit of the normalised $g^{(2)}$ data, which has the following form:

$$g^{(2)}(\tau)=A\text{-}Be^{\kappa_{21}\tau}+Ce^{\kappa_{23/31}\tau}, \quad (1)$$

where A, B, and C are fitting coefficients and solving for the excited state (i.e. total) decay rate κ_{21} and nonradiative (i.e. bunching corresponding to the metastable state) decay rate $\kappa_{23/31}$. The fit was determined by minimising the least squares error between the model in Equation (1) and the normalised $g^{(2)}$ data. Here, τ is the measured time between photon emission events or delay time. For antibunched light, indicative of a single-photon emitter, it must satisfy the condition of $g^{(2)}(0)<0.5$. Figure 3B shows the fit for the excited state decay rate (κ_{21}) as a function of pump power. The linear relationship provides the zero-power decay rate at zero pump power, i.e. $\tau_{21}(P=0)=1/\kappa_{21}(P=0)$, where P is the pump power. We found for this optical defect an excited state lifetime of τ_{21}=7 ns and a nonradiative lifetime of $\tau_{23/31}$=5 µs. The other quantum emitters shown in the spectra of Figure 2B (purple, black, and blue lines) were found to be two-level emitters. The fit for the two-level model is just like the three-level model with the third term of the right-hand side of Equation (1) omitted. The purple, black, and blue defects yielded excited state lifetimes of 2.17, 4.43, and 7.93 ns, with $g^{(2)}(0)$ values of 0.045, 0.036, and 0.150, respectively. The excited state lifetimes of the ZnO NP defects were comparable to previously reported work [22–26].

We also performed power saturation measurements to determine the limit of the pump power that would yield the maximum count rate attainable from the bright emitter. A saturation curve for the emitter can be seen in Figure 3C, where the power is increased towards 5.7 mW, and the emission rate R begins to saturate. We fit emission rate versus pump power relationship according to $R(P)=R_{sat}P/(P+P_{sat})$, where P_{sat} is the saturated power, to find the saturated emission rate R_{sat}. Fitting this yields a value of R_{sat}=1.05 Mc/s for P_{sat}=1.26 mW. This saturation power is 20 times higher than previously reported ZnO single-photon emitters without an irreversible ionisation of the defect [22]. A comparison of saturated power and count rate for this bright emitter and the defect reported by Choi et al. [23] reveals that the powers are comparable with a count rate one order of magnitude greater. These results in conjunction with photon statistics show that ZnO defects [22–26] are comparable to other room-temperature single-photon emitters, namely, optical defects in diamond [55] and silicon carbide [20].

3.2 Optical characterisation of ZnO NPs deposited on a silicon substrate

ZnO NPs were removed (see Section 2.4) from the silica substrate to see if their optical characteristics were retained after redeposition onto a silicon substrate. This sample was investigated using scanning confocal microscopy (see Section 2.2) again, and a typical 10×10 µm² confocal scan of ZnO NPs on the Si substrate is shown below in Figure 4A. From this confocal scan, optically distinct rounded features, indicative of optical defects within ZnO NPs, were again observed. A further optical characterisation was performed on the defect shown in Figure 4A.

The spectrum for the circled defect is shown in Figure 4B, highlighting a distinct emission peak at 630 nm with a subtle peak at 570 nm. The sharp emission peak could have become more resolvable due to the suppression of the fluorescence from the phonon sideband from 650 to 700 nm. The suppression of phonon sidebands is not uncommon and has been observed for nitrogen vacancy colour centres within nanodiamond when they were deposited on an SiO_2/Si substrate [56]. However, this suppression was not observed when Zhao et al. [56] recorded their PL spectrum at room temperature. Comparing the spectra for Si and SiO_2 (Figure 2B) substrates, there does not seem to be a sharp and distinct emission peak in the latter's spectra. This means it is possible that we are

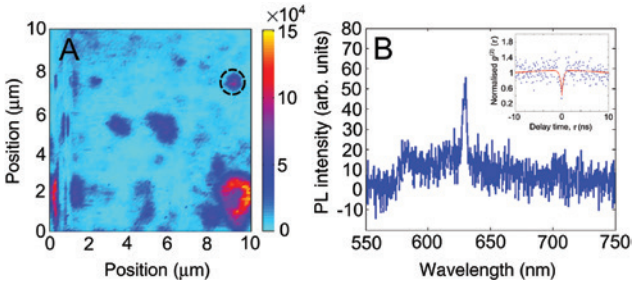

Figure 4: (A) Representative 10×10 µm² confocal scan of the 700°C annealed ZnO NPs removed from the SiO_2 substrate and redeposited onto a Si substrate. The optical defect in the centre of the dashed circle was characterised. (B) Spectrum of the circled defect. The integration time was 30 s and was chosen due to a concern that the defect would photobleach. The inset shows the normalised $g^{(2)}$ histogram (blue points) along with a three-level model fit (red line) at a pump power of 0.67±5×10⁻³ mW. The time bin was 512 ps, with an integration time of 600 s, and the count rates at the detectors were 7 and 20 kc/s with a background count of 2 kc/s [19].

observing another type of emitter. Furthermore, contrasting spectral features can be the result of a change in the local refractive index environment. The inset of Figure 4B shows a three-level model fit with $g^{(2)}(0)=0.42$, excited state lifetime of 1.20 ns, and nonradiative lifetime of 9.17 ns.

The optical characterisation of the processed sample shows that these ZnO NPs were able to be removed and still exhibit single-photon emission and visible fluorescence. It should be noted that the bright defects reported in this study were rare for both SiO_2 and Si substrates. Many diffraction-limited weak emitters were observed, which did not yield quantum behaviour (e.g. the other fluorescent features not at the centre of the cross hair). To increase the statistics of depositing ZnO NPs onto the Si substrate, the preparation method could be modified to an evaporation process. The NP and IPA mixture can be evaporated on a hotplate, which is a less energetic method than spinning, and this will increase the number of NPs deposited onto the substrate.

Removing the NPs from the SiO_2 growth substrate is an example where the optical environment can influence the emission properties of an encapsulated emitter. This has been explored for dipole emission within an NP in a generalised refractive index distribution [57] and experimentally tested with PMMA coatings of a nanodiamond, containing single emitters, on a Si substrate [58]. Furthermore, the removal and redeposition onto a Si substrate compromises the ability to address the same emitters. This can result in a substantial difference in the count rates between SiO_2 and Si substrates, as we may be observing fundamentally different emitters.

3.3 ZnO NP uptake by HaCaT cells

ZnO NPs rather than larger particles are routinely used by manufacturers in sunscreens in the skin care industry due to its wide bandgap (3.3 eV at room temperature), which makes it readily absorb radiation in the UV spectrum. In addition, ZnO NPs have many therapeutic properties [45–48], and in general, NPs show great potential for bioimaging applications [49]. Fluorescent ZnO nanomaterials have already been touted as a promising candidate for bioimaging and biosensing platforms based on different morphologies [59–61]. However, *in vitro* photostability has been an issue, which can be only resolved by multiple coatings [61]. Here, we present the intrinsic fluorescence from our ZnO NPs that can be used for *in vitro* imaging.

ZnO NPs were removed in a similar manner as discussed in Section 2.4 using distilled water instead of IPA. A dynamic light scattering (DLS) measurement was performed on the NPs suspended in distilled water, which yielded a strong signal that indicated a particle size of up to 2500 nm. This particle size is unusually large when compared to NPs measuring tens of nanometres on the surface of the silica substrate. However, ZnO NPs have been observed to aggregate into sizes in the order of thousands of nanometres in sodium chloride and sodium phosphate solutions, both constituents of PBS [62]. These ZnO NP aggregate sizes are well within the range that was observed in the DLS measurements.

Human epidermal keratinocyte (HaCaT) cells were chosen for the uptake of the ZnO NP aggregates, which can be seen for an individual HaCaT cell in a bright-field image of Figure 5A and wide-field fluorescent image of Figure 5B. The cells were prepared as described in Section 2.4. The circular shape of the cell is an indication that the cell may have died, and in contrast, a healthy cell will have branch-like structures emanating from the cellular membrane and cytoplasm. Dead cells have a larger autofluorescence signal compared to healthy cells. If the defect signal within a healthy cell is above this autofluorescence, it can be easily detected.

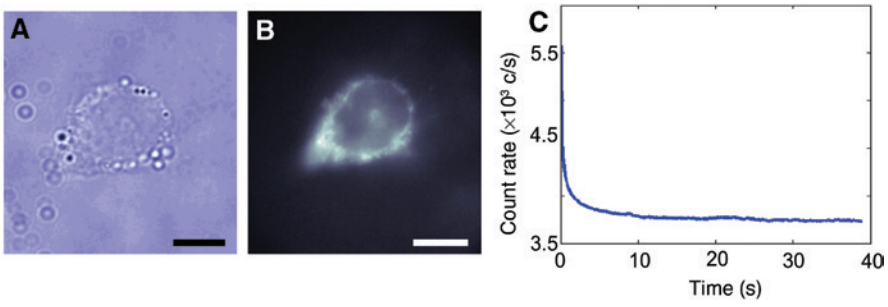

Figure 5: (A) Representative bright-field microscope image of an untreated HaCaT cell. (B) Wide-field confocal fluorescence of the same untreated HaCaT cell. The scale bars are 10 μm in length. (C) Corresponding count trace for the untreated HaCaT cell, from wide-field confocal modality, showing typical bleaching of the cell's autofluorescence.

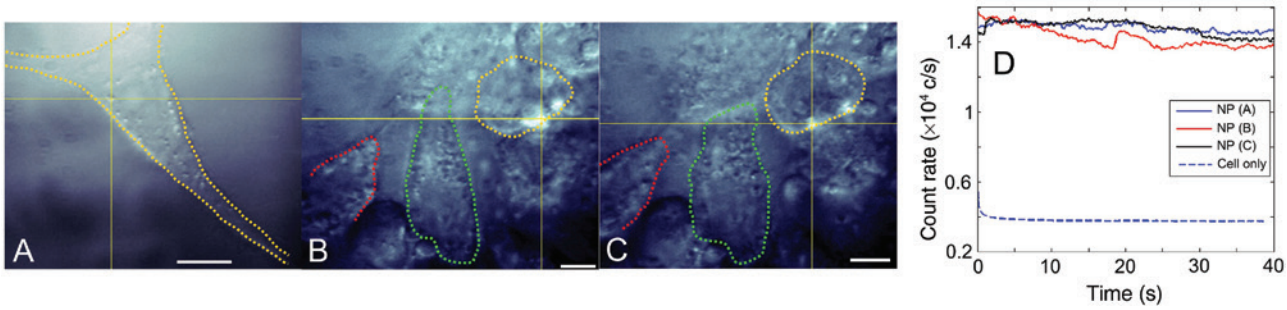

Figure 6: Wide-field confocal fluorescence images of the (A) filtered and (B and C) unfiltered ZnO NP solution in PBS *in vitro*. The contours of some cells have been highlighted with dashed lines as a reference. The scale bars are 10 μm in length. (D) Count traces were obtained at the centre of the cross hairs with 4×4 pixel area binning of the intensity, where the blue, red, and black lines represent the count traces from A to C. The blue dashed line is also shown as a comparison to emphasise the photobleaching behaviour of the HaCaT cell only from Figure 5C. The count traces were obtained within the wide-field confocal modality.

Figure 5C is the count trace for the HaCaT cell shown in Figure 5A and B, which shows almost immediate photobleaching behaviour in its photodynamics. This acts as a reference point for the background count rate of approximately 3.7 kc/s, after 30–40 s, when trying to differentiate the ZnO NP emission from the cell's autofluorescence. For more experimental details on how the cells were imaged, see Section 2.6.

Figure 6 shows representative wide-field fluorescence images of treated HaCaT cells suspended in PBS, where Figure 6A is for filtered (using 0.22 μm filter) and Figure 6B and C is for unfiltered ZnO NP solutions. For the unfiltered solution, two ZnO NP aggregrates were observed to have been taken up by the same HaCaT cell. Figure 6D show the corresponding count traces (blue, red, and black lines) of the NPs found in Figure 6A–C along with the count trace for the untreated HaCaT cell from Figure 5C (blue dashed line). It must be noted that, in high enough concentration, ZnO NPs have been shown to be cytotoxic [63, 64].

The count traces show photostability from an optical defect within the ZnO NP and they all show an average count rate that was above the photobleaching level of the untreated HaCaT cell. The average stable count rate of approximately 1.5×10^4 c/s was three times greater than the photobleaching count rate of the untreated cells at approximately 4 kc/s. This difference can only be due to ZnO NPs, which have been taken up by the HaCaT cells, as PBS has the same count rate behaviour as for the HaCaT cells only. The stable count rate may be due to the power density being lower in these cell experiments whilst using the wide-field modality, which is equivalent to a low-power measurement in noncell confocal imaging of Section 2.2. These results for filtered and unfiltered ZnO NP solutions demonstrate that ZnO NPs have been taken up by the HaCaT cells and show that the intrinsic fluorescent properties of ZnO NP optical defects can potentially act as a biomarker.

4 Conclusions

Room-temperature single-photon emission has been observed from optical defects within ZnO NPs derived from ion implantation followed by thermal oxidation at 700°C of a silica substrate. Red luminescence of quantum emission from ZnO NP optical defects within a bandwidth of 580–875 nm have been attributed to multiple emissions peaks. These defects also show relative photostability, which enables sufficient time for investigation of their fluorescence properties. Furthermore, we have shown that these ZnO NPs were resilient to removal from their original substrate. Subsequently, NPs were taken up by human keratinocyte HaCaT cells with *in vitro* photostability observed. This research opens up new avenues for the identification of ZnO optical defects in the visible region. Stable fluorescence of these defects has great advantages for various applications, ranging from quantum to biomedical.

Acknowledgments: K.C. acknowledges a Melbourne Research Scholarship awarded by The University of Melbourne (UoM). B.C.G. acknowledges an ARC Future Fellowship (FT110100225). S.T.-H. acknowledges an ARC Australian Research Fellowship (DP1096288), an UoM Interdisciplinary Seed Grant, and the National Institute for Materials Science for travel support. H.A. was supported by JSPS-KAKENHI 26390032.

References

[1] Wu J, Cao J, Han WQ, Janotti A, Kim HC. Functional metal oxide nanostructures. New York, USA: Springer, 2012.

[2] Niederberger M, Pinna N. Metal oxide nanoparticles in organic solvents: synthesis, formation, assembly and application. London, UK: Springer, 2009.

[3] Jagadish C, Pearton SJ. Zinc oxide bulk, thin films and nanostructures: processing, properties, and applications. Oxford, UK: Elsevier, 2011.

[4] Özgür U, Alivov YI, Liu C, Teke A, Reshchikov MA, Doğan S, Avrutin V, Cho SJ, Morkoç H. A comprehensive review of ZnO materials and devices. J Appl Phys 2005;98:041301.

[5] Kim KH, Park KC, Ma DY. Structural, electrical and optical properties of aluminum doped zinc oxide films prepared by radio frequency magnetron sputtering. J Appl Phys 1997:81:7764.

[6] Ellmer K. Resistivity of polycrystalline zinc oxide films: current status and physical limit. J Phys D Appl Phys 2001;34:3097–108.

[7] Wu JJ, Liu SC. Low-temperature growth of well-aligned ZnO nanorods by chemical vapor deposition. Adv Mater 2002;14:215–8.

[8] Ko HJ, Chen YF, Zhu Z, Yao T, Kobayashi I, Uchiki H. Photoluminescence properties of ZnO epilayers grown on CaF_2 (111) by plasma assisted molecular beam epitaxy. Appl Phys Lett 2000;76:1905.

[9] Kato H, Sano M, Miyamoto K, Yao T. Growth and characterization of Ga-doped ZnO layers on a-plane sapphire substrates grown by molecular beam epitaxy. J Cryst Growth 2002;237–239:538–43.

[10] Yu J, Yu X. Hydrothermal synthesis and photocatalytic activity of zinc oxide hollow spheres. Environ Sci Technol 2008;42:4902–7.

[11] Tam KH, Cheung CK, Leung YH, Djurišić AB, Ling CC, Beling CD, Fung S, Kwok WM, Chan WK, Phillips DL, Ding L, Ge WK. Defects in ZnO nanorods prepared by a hydrothermal method. J Phys Chem B 2006;110:20865–71.

[12] Janotti A, Van de Walle CG. Fundamentals of zinc oxide as a semiconductor. Rep Prog Phys 2009;72:126501.

[13] Vayssieres L. Growth of arrayed nanorods and nanowires of ZnO from aqueous solutions. Adv Mater 2003;15:464–6.

[14] Wang ZL, Kong XY, Zuo JM. Induced growth of asymmetric nanocantilever arrays on polar surfaces. Phys Rev Lett 2003;91:185502.

[15] Meulenkamp EA. Synthesis and growth of ZnO nanoparticles. J Phys Chem B 1998;102:5566–72.

[16] Djurišić AB, Leung YH. Optical properties of ZnO nanostructures. Small 2006;2:944–61.

[17] Lin B, Fu Z, Jia Y. Green luminescent center in undoped zinc oxide films deposited on silicon substrates. Appl Phys Lett 2001;79:943–5.

[18] Kohan AF, Ceder G, Morgan D, Van de Walle CG. First-principles study of native point defects in ZnO. Phys Rev B 2000;61:15019–27.

[19] Brouri R, Beveratos A, Poizat JP, Grangier P. Photon antibunching in the fluorescence of individual color centers in diamond. Opt Lett 2000;25:1294–6.

[20] Castelletto S, Johnson BC, Ivády V, Stavrias N, Umeda T, Gali A, Ohshima T. A silicon carbide room-temperature single-photon source. Nat Mater 2014;13:151–6.

[21] Michler P, Imamoglu A, Mason MD, Carson PJ, Strouse GF, Buratto SK. Quantum correlation among photons from a single quantum dot at room temperature. Nature 2000;406:968–70.

[22] Morfa AJ, Gibson BC, Karg M, Karle TJ, Greentree AD, Mulvaney P, Tomljenovic-Hanic S. Single-photon emission and quantum characterization of zinc oxide defects. Nano Lett 2012;12:949–54.

[23] Choi S, Johnson BC, Castelletto S, Ton-That C, Phillips MR, Aharonovich I. Single photon emission from ZnO nanoparticles. Appl Phys Lett 2014;104:261101.

[24] Choi S, Berhane AM, Gentle A, Ton-That C, Phillips MR, Aharonovich I. Electroluminescence from localized defects in zinc oxide: toward electrically driven single photon sources at room temperature. ACS Appl Mater Interfaces 2015;7:5619–23.

[25] Jungwirth NR, Pai YY, Chang HS, Macquarrie ER, Nguyen KX, Fuchs GD. A single-molecule approach to ZnO defect studies: single photons and single defects. J Appl Phys 2014;116:043509.

[26] Neitzke O, Morfa A, Wolters J, Schell AW, Kewes G, Benson O. Investigation of line width narrowing and spectral jumps of single stable defect centers in ZnO at cryogenic temperature. Nano Lett 2015;15:3024–9.

[27] Djurišić AB, Leung YH, Tam KH, Hsu YF, Ding L, Ge WK, Zhong YC, Wong KS, Chan WK, Tam HL, Cheah KW, Kwok WM, Phillips DL. Defect emissions in ZnO nanostructures. Nanotechnology 2007;18:095702.

[28] Vanheusden K, Warren WL, Seager CH, Tallant DR, Voigt JA, Gnade BE. Mechanisms behind green photoluminescence in ZnO phosphor powders. J Appl Phys 1996;79:7983.

[29] Meng XQ, Shen DZ, Zhang JY, Zhao DX, Lu YM, Dong L, Zhang ZZ, Liu YC, Fan XW. The structural and optical properties of ZnO nanorod arrays. Solid State Commun 2005;135:179–82.

[30] Ng HT, Chen B, Li J, Han J, Meyyappan M, Wu J, Li SX, Haller EE. Optical properties of single-crystalline ZnO nanowires on m-sapphire. Appl Phys Lett 2003;82:2023.

[31] Chen Z, Wu N, Shan Z, Zhao M, Li S, Jiang CB, Chyu MK, Mao SX. Effect of N_2 flow rate on morphology and structure of ZnO nanocrystals synthesized via vapor deposition. Scr Mater 2005;52:63–7.

[32] Yang Q, Tang K, Zuo J, Qian Y. Synthesis and luminescent property of single-crystal ZnO nanobelts by a simple low temperature evaporation route. Appl Phys A 2004;79:1847–51.

[33] Wang ZG, Zu XT, Zhu S, Wang LM. Green luminescence originates from surface defects in ZnO nanoparticles. Phys E Low-Dimens Syst Nanostruct 2006;35:199–202.

[34] Liu X, Wu X, Cao H, Chang R. Growth mechanism and properties of ZnO nanorods synthesized by plasma-enhanced chemical vapor deposition. J Appl Phys 2004;95:3141–7.

[35] Fabbri F, Villani M, Catellani A, Calzolari A, Cicero G, Calestani D, Calestani G, Zappettini A, Dierre B, Sekiguchi T, Salviati G. Zn vacancy induced green luminescence on non-polar surfaces in ZnO nanostructures. Sci Rep 2014;4:5158.

[36] McCluskey MD, Jokela SJ. Defects in ZnO. J Appl Phys 2009;106:071101.

[37] Reshchikov MA, Morkoç H, Nemeth B, Nause J, Xie J, Hertog B, Osinsky A. Luminescence properties of defects in ZnO. Phys B Condens Matter 2007;401–402:358–61.

[38] Studenikin S, Golego N, Cocivera M. Fabrication of green and orange photoluminescent, undoped ZnO films using spray pyrolysis. J Appl Phys 1998;84:2287–94.

[39] Greene LE, Law M, Goldberger J, Kim F, Johnson JC, Zhang Y, Saykally RJ, Yang P. Low-temperature wafer-scale production of ZnO nanowire arrays. Angew Chem 2003;42:3031–4.
[40] Kaftelen H, Ocakoglu K, Thomann R, Tu S, Weber S, Erdem E. EPR and photoluminescence spectroscopy studies on the defect structure of ZnO nanocrystals. Phys Rev B 2012;86:1–9.
[41] Chen YN, Xu SJ, Zheng CC, Ning JQ, Ling FCC, Anwand W, Brauer G, Skorupa W. Nature of red luminescence band in research-grade ZnO single crystals: a "self-activated" configurational transition. Appl Phys Lett 2014;105:041912.
[42] Amekura H, Umeda N, Sakuma Y, Kishimoto N, Buchal C. Fabrication of ZnO nanoparticles in SiO_2 by ion implantation combined with thermal oxidation. Appl Phys Lett 2005;87:013109.
[43] Amekura H, Umeda N, Sakuma Y, Plaksin OA, Takeda Y, Kishimoto N, Buchal C. Zn and ZnO nanoparticles fabricated by ion implantation combined with thermal oxidation, and the defect-free luminescence. Appl Phys Lett 2006;88:153119.
[44] Wang ZL. Zinc oxide nanostructures: growth, properties and applications. J Phys Condens Matter 2004;16:R829–58.
[45] Rasmussen JW, Martinez E, Louka P, Wingett DG. Zinc oxide nanoparticles for selective destruction of tumor cells and potential for drug delivery applications. Expert Opin Drug Deliv 2011;7:1063–77.
[46] Guo D, Wu C, Jiang H, Li Q, Wang X, Chen B. Synergistic cytotoxic effect of different sized ZnO nanoparticles and daunorubicin against leukemia cancer cells under UV irradiation. J Photochem Photobiol B Biol 2008;93:119–26.
[47] Reddy KM, Feris K, Bell J, Wingett DG, Hanley C, Punnoose A. Selective toxicity of zinc oxide nanoparticles to prokaryotic and eukaryotic systems. Appl Phys Lett 2007;90:2013–6.
[48] Seil JT, Webster TJ. Antibacterial effect of zinc oxide nanoparticles combined with ultrasound. Nanotechnology 2012;23:495101.
[49] Sharma P, Brown S, Walter G, Santra S, Moudgil B. Nanoparticles for bioimaging. Adv Colloid Interface Sci 2006;123–126:471–85.
[50] Liu YX, Liu YC, Shen DZ, Zhong GZ, Fan XW, Kong X, Mu R, Henderson DO. Preferred orientation of ZnO nanoparticles formed by post-thermal annealing zinc implanted silica. Solid State Commun 2002;121:531–6.
[51] Xiong HM. ZnO nanoparticles applied to bioimaging and drug delivery. Adv Mater 2013;25:5329–35.
[52] Wang XJ, Vlasenko LS, Pearton SJ, Chen WM, Buyanova IA. Oxygen and zinc vacancies in as-grown ZnO single crystals. J Phys D Appl Phys 2009;42:175411.
[53] Weber JR, Koehl WF, Varley JB, Janotti A, Buckley BB, Van de Walle CG, Awschalom DD. Quantum computing with defects. Proc Natl Acad Sci USA 2010;107:8513–8.
[54] Kitson S, Jonsson P, Rarity J, Tapster P. Intensity fluctuation spectroscopy of small numbers of dye molecules in a microcavity. Phys Rev A 1998;58:620–7.
[55] Aharonovich I, Castelletto S, Simpson DA, Su CH, Greentree AD, Prawer S. Diamond-based single-photon emitters. Rep Prog Phys 2011;74:076501.
[56] Zhao HQ, Fujiwara M, Takeuchi S. Suppression of fluorescence phonon sideband from nitrogen vacancy centers in diamond nanocrystals by substrate effect. Opt Express 2012;20:15628–35.
[57] Chung K, Tomljenovic-Hanic S. Emission properties of fluorescent nanoparticles determined by their optical environment. Nanomaterials 2015;5:895–905.
[58] Khalid A, Chung K, Rajasekharan R, Lau DWM, Karle TJ, Gibson BC, Tomljenovic-Hanic S. Lifetime reduction and enhanced emission of single photon color centers in nanodiamond via surrounding refractive index modification. Sci Rep 2015;5:11179.
[59] Hahm J. Zinc oxide nanomaterials for biomedical fluorescence detection. J Nanosci Nanotechnol 2014;14:475–86.
[60] Yu H, Wong MKF, Ali EM, Ying JY. Photostable and luminescent ZnO films: synthesis and application as fluorescence resonance energy transfer donors. Chem Commun 2008:4912–4.
[61] Kamińska I, Sikora B, Fronc K, Dziawa P, Sobczak K, Minikayev R, Paszkowicz W, Elbaum D. Novel ZnO/MgO/Fe_2O_3 composite optomagnetic nanoparticles. J Phys Condens Matter 2013;25:194105.
[62] Ng AMC, Chan CMN, Guo MY, Leung YH, Djurišić AB, Hu X, Chan WK, Leung FCC, Tong S. Antibacterial and photocatalytic activity of TiO_2 and ZnO nanomaterials in phosphate buffer and saline solution. Appl Microbiol Biotechnol 2013;97:5565–73.
[63] Lee SH, Lee HR, Kim YR, Kim MK. Toxic response of zinc oxide nanoparticles in human epidermal keratinocyte HaCaT cells. Toxicol Environ Health Sci 2012;5:14–8.
[64] Sharma V, Shukla RK, Saxena N, Parmar D, Das M, Dhawan A. DNA damaging potential of zinc oxide nanoparticles in human epidermal cells. Toxicol Lett 2009;185:211–8.